

THE EXCHANGE OF MASS AND ANGULAR MOMENTUM IN THE IMPACT EVENT OF ICE GIANT PLANETS: IMPLICATIONS FOR THE ORIGIN OF URANUS

KENJI KUROSAKI¹ AND SHU-ICHIRO INUTSUKA¹

¹*Department of Physics, Nagoya University, Chikusa-ku, Nagoya 464-8602, Japan*

(Received May 31, 2018; Revised September 12, 2018; Accepted November 13, 2018)

ABSTRACT

Uranus has a tilted rotation axis, which is supposed to be caused by a giant impact. In general, an impact event also changes the internal compositional distribution and drives mass ejection from the planet, which may provide the origin of satellites. Previous studies of the impact simulation of Uranus investigated the resultant angular momentum and the ejected mass distribution. However, the effect of changing the initial condition of the thermal and compositional structure is not studied. In this paper, we perform hydrodynamics simulations for the impact events of Uranus-size ice giants composed of a water core surrounded by a hydrogen envelope using two variant methods of the smoothed particle hydrodynamics. We find that the higher entropy target loses its envelope more efficiently than the low entropy target. However, the higher entropy target gains more angular momentum than the lower entropy target since the higher entropy target has more expanded envelope. We discuss the efficiency of angular momentum transport and the amount of the ejected mass and find a simple analytical model to roughly reproduce the outcomes of numerical simulations. We suggest the range of possible initial conditions for the giant impact on proto-Uranus that reproduces the present rotation tilt of Uranus and sufficiently provides the total angular momentum of the satellite system that can be created from the fragments from the giant impact.

Keywords: planets and satellites: gaseous planets — planets and satellites: individual (Uranus) — planets and satellites: formation

1. INTRODUCTION

Our solar system has two ice giants, Uranus and Neptune, that are supposed to be mainly composed of gas envelope, icy mantle and solid core from the top to the bottom (e.g. Hubbard & Macfarlane 1980; Helled et al. 2011; Nettelmann et al. 2016). These two planets have similar mass and radius, while their spin axes, satellite systems, and intrinsic luminosities are different. For example, the obliquity of Uranus is 98° , while that of Neptune is 27.7° . Safronov (1966) pointed out that Uranus experienced a giant impact event to reproduce its tilted rotation axis. An impactor of several earth mass may have transported the angular momentum to proto-Uranus via collision and tilted the rotation axis of proto-Uranus. Parisi & Brunini (1997) estimated the giant impact based on the conservation of angular momentum and energy and concluded that the minimum impactor mass is $\sim 1 - 1.1M_\oplus$. Such large impact event may also have produce a circumplanetary disk around the proto-Uranus, which might be the origin of small prograde satellites around Uranus (e.g., Parisi et al. 2008). A giant impact scenario is widely accepted as an explanation for terrestrial moon formation (Hartmann & Davis 1975; Cameron & Ward 1976) and recently suggested to apply to Phobos and Deimos formation (e.g., Citron et al. 2015; Hyodo et al. 2017a). Since the impact event causes erosion of proto-Uranus, the angular momentum that impactor brings is redistributed to proto-Uranus and eroded gas envelope and fragments around the proto-Uranus. The internal compositional distribution after the impact is unknown because the mixing process by the impact event is a highly non-linear problem to analyze theoretically. Moreover, the impact event is also essential to the thermal evolution. Present Uranus has a low intrinsic luminosity comparing to Neptune. Nettelmann et al. (2016) explained the luminosity of Uranus considering a thermal boundary layer between an outer H-He-rich envelope and an inner ice-rich layer. If a giant impact event occurs, internal compositional distribution should be changed. If the mixing of icy material in the H_2/He envelope is efficient, the thermal evolution is expected to be accelerated (Kurosaki & Ikoma 2017).

The giant impact simulations on rock-composed protoplanets have been systematically calculated (Marcus, et al. 2009; Genda, et al. 2012). Those studies have not considered the atmosphere. The atmosphere is eroded more efficiently than rock materials because the thermal pressure of gas is more sensitive than that of rock materials. Impact events on Uranus have been investigated by use of hydrodynamical simulation. Korycansky et al. (1990) studied a giant impact on ice giant for the first time. They calculated one-dimensional spherically symmetric hydrodynamic simulation and investigated the H_2/He envelope erosion due to the impact. They found a sharp transition between the cases of nearly complete retention and dispersal of H_2/He envelope, which depend on the amount of energy deposition on the envelope. Three-dimensional hydrodynamical simulations are done by Slattery et al. (1992) and Kegerreis et al. (2018). Slattery et al. (1992) used the smoothed particle hydrodynamic simulation (hereafter SPH simulation) to constrain the angular momentum of proto-Uranus and eroded mass after the giant impact.

Previous work constrained the impactor mass to explain the amount of the present angular momentum of Uranus. In the context of thermal evolution of Uranus, the evolutionary stage at time of the giant impact is also important. When the age of proto-Uranus is younger than 10^8 years, the H_2/He envelope still remains extended and the efficiency of the gas envelope erosion will be increased. It should be useful to study the effect of changing the structure of the proto-Uranus on the result of giant impact to constrain the evolutionary stage of the proto-Uranus at the time of the giant impact event.

In this paper, we study the impact event on a proto-Uranus. The aim of this paper is to investigate the envelope erosion and the efficiency of angular momentum transport to the proto-Uranus. Since there are no constraints on the age of Uranus at the time of the impact event, we consider two extreme cases: an impact onto a young (10^8 years) ice giant, when it was in a high-temperature state, and an impact onto a mature ice giant (10^9 years), when it was in a low-temperature state.

Section 2 describes the methods and settings for our simulation. The results of our study are described in Section 3 and discussions in Section 4. We summarize the conclusion of our study in section 5.

2. METHOD

We use Godunov-type smoothed particle hydrodynamical calculation, hereafter GSPH, (Inutsuka 2002; Sugiura & Inutsuka 2016) to solve the following hydrodynamic equations:

$$\frac{d\rho}{dt} = -\rho \nabla \cdot \mathbf{v} \quad (1)$$

$$\frac{d\mathbf{v}}{dt} = -\frac{1}{\rho} \nabla P + \nabla \int dx'^3 \frac{G\rho(x')}{|\mathbf{x} - \mathbf{x}'|} \quad (2)$$

$$\frac{du}{dt} = -\frac{P}{\rho} \nabla \cdot \mathbf{v} \quad (3)$$

$$P = P(\rho, u) \quad (4)$$

where ρ , P , \mathbf{v} and u are density, pressure, velocity, and specific internal energy, respectively. t is the time, \mathbf{x} is the position, and $G(= 6.67408 \times 10^{-8} \text{ cm}^3 \text{ g}^{-1} \text{ s}^{-2})$ is the gravitational constant. The method has advantages on tracing strong shock and contact discontinuity (Cha et al. 2010). We introduce the exact and spatially second-order Riemann solver for piece-wise polytropic gas to our GSPH. As for the equation of state (Eq. 4), we use Saumon et al. (1995) for hydrogen and helium, and SESAME 7150 for water (Lyon & Johnson 1992). To implement non-ideal equation of states in GSPH, the effective heat ratio γ_{eff} is calculated from the data table of non-ideal equation of state. We also take into account the gravity force on Riemann solver (Guo et al. 2018, submitted). We have implemented the acceleration modules for our SPH code with FDPS (Iwasawa et al. 2016) and FDPS fortran interface (Namekata et al. 2018). We have tested our SPH code by reproducing the analytical solution for a shock tube and the Lane-Emden solution for a polytrope gas equilibrium spheres.

2.1. Initial conditions for target and impactor

In this paper, we fix following two parameters. We assume masses of target and impactor are $13 M_{\oplus}$ and $1 M_{\oplus}$, respectively. The target is composed of 20 % of hydrogen and 80 % of water. The impactor is composed of 100 % of water. The impact angle, hereafter θ , is assumed to 15° , 30° , 45° , and 60° . The impact position is $(R_p + r_{\text{imp}}) \sin \theta$, where R_p and r_{imp} are radii of target and impactor, respectively. The impact velocity is assumed to be the escape velocity, which is represented by $v_{\text{imp}} = \sqrt{2GM_p/R_p}$ ¹ where M_p is the target mass, and m_{imp} is the impactor mass. The impact velocities are $1.68 \times 10^4 \text{ m s}^{-1}$ and $1.85 \times 10^4 \text{ m s}^{-1}$ for the HT and LT target discussed below,

¹ Based on the two-body problem, the impact velocity is equal to $v_{\text{imp},2} = \sqrt{2G(M_p + m_{\text{imp}})/(R_p + r_{\text{imp}})}$. The adopted impact velocity (v_{imp}) is faster than $v_{\text{imp},2}$ by 10 %.

respectively. Those impact velocities correspond to the free-fall motion from infinity. The escape velocity of the target depends on the target’s radius. Since the HT target has a larger radius than the LT target, its escape velocity is lower. Here we assume that both the target and impactor are not spinning before the collision, as in [Slattery et al. \(1992\)](#) and [Kegerreis et al. \(2018\)](#). We also investigate the effect of changing temperature structure of the target on the outcome of the giant impact. Here we assume two types of target. The high temperature target, hereafter HT, is assumed to have entropy $S = S(100 \text{ bar}, 1000 \text{ K})$, while the low temperature target, hereafter LT, is assumed its entropy $S = S(100 \text{ bar}, 500 \text{ K})$. [Table 1](#) shows the parameters for the target and impactor. Both the HT and the LT target are warmer than present Uranus. The age of LT target is 10^9 years, while HT target is 10^8 years (see [Appendix B](#)). The target [Kegerreis et al. \(2018\)](#) adopted is equivalent to the present Uranus. If the rotation period of the target is longer than ~ 100 hours, the target’s angular momentum is smaller than the present Uranus by an order of magnitude and the initial target’s spin can be ignored. If the target’s angular momentum is comparable to the present Uranus, the rotating H-He atmosphere changes its impact mach number and hence the resulting internal angular momentum distribution. However, it is beyond the scope of this study. We assume that the target’s angular momentum is much smaller than that provided by impactor for simplicity. Hereafter we discuss the spin of the target that is the result of the impact.

We stop the numerical simulation at $t = 10 t_{\text{ff}}$, where t_{ff} is the free fall time of the target given by $t_{\text{ff}} = \sqrt{\pi^2 R_p^3 / (8GM_p)}$. t_{ff} for HT and LT are 0.95 hours and 0.71 hours, respectively. Thus we stop HT and LT simulations at 9.5 hours and 7.1 hours, respectively. In this case, the number of timesteps in our simulations are only on the order of 10^3 thanks to the efficiency of GSPH.

	Mass [g]	Radius [cm]	Temperature [K]	H ₂ [wt %]	H ₂ O [wt %]	Particles
HT	7.82×10^{28}	3.18×10^9	1000 K (100 bar)	20	80	65500
LT	7.82×10^{28}	3.03×10^9	500 K (100 bar)	20	80	65500
Impactor	5.97×10^{27}	1.13×10^9	300 K (1 bar)	0	100	5000

Table 1. Conditions for HT target, LT target, and impactor for our simulation.

3. RESULTS

In this section, we show results of our impact simulations. [Figure 1](#) shows four snapshots of the impact simulation for HT whose impact angle is 30° , which represent the initial condition ($t = 0$), $t = t_{\text{ff}}$, $t = 2 t_{\text{ff}}$, and $t = 8 t_{\text{ff}}$. When the impactor collides on the target, the impactor gives its momentum to the hydrogen envelope of the target. In the case of $\theta = 30^\circ$, the impactor collide with the H₂O core of the target. After the collision, the impactor fall onto the target’s core and the hydrogen envelope is eroded due to the collision.

Here we introduce the definition for the eroded particle from the target at $t = 10 t_{\text{ff}}$ after the collision. The mass, position, velocity, and internal energy of i -th particle are m_i , \mathbf{r}_i , \mathbf{v}_i and u_i , respectively. After the impact, the hydrogen gas expands around the target. Eroded gas particles have enough energy to escape from the target and their positions are outside of the target. In this

study, the eroded particle condition is

$$\frac{1}{2}m_i|\mathbf{v}_i|^2 - m_i \sum_{i \neq j} \frac{Gm_j}{|\mathbf{r}_i - \mathbf{r}_j|} > 0 \quad (5)$$

$$|\mathbf{r}_i - \mathbf{R}_{t,c}| > R_p \quad (6)$$

where $\mathbf{R}_{t,c}$ is the position of the center of the target.

Figure 2 and 3 show the eroded region after the collision for the high temperature target and low temperature target, respectively. The eroded region for hydrogen and water is shown in orange and yellow, respectively. Those figures show the z-plane cross sections of the results by choosing the particles in the range of $z = [-0.1, 0.1]$. We can find that the property of the mass erosion changes depending on whether the impactor collides with the target core or not. When the impactor collides with the core, the impactor change its trajectory and the hydrogen envelope is eroded along the impactor's trajectory. In the case of impact angle is 15° and 30° , the impactor collide with the water core of the target. On the other hand, the impactor does not collide with the water core in the case of impact angle is 45° and 60° . After the collision, the impactor is captured in the target while part of the hydrogen envelope of the target receives energy and angular momentum from the impactor and escapes from the target.

Figure 5 shows the relationship between the eroded mass and impact parameter for HT and LT case. In HT case, the eroded mass is larger than LT case. That is because the volume of hydrogen envelope of HT case is larger than that of LT case and the escaped region of HT case is also larger than LT case. Moreover, the escape velocity at the surface of HT is smaller than LT, which promotes the ejection of particles from the target. After the collision, the minimum masses of H-He retained for HT and LT are 80 % and 90 %, respectively, while [Kegerreis et al. \(2018\)](#) obtain 75 %. The difference is due to the equation of states for hydrogen-helium. The adopted equations of states for hydrogen helium ([Saumon et al. 1995](#)) in our calculation have smaller heat capacity ratio compared to that of [Hubbard & Macfarlane \(1980\)](#). That is, in our calculation, the pressure response against density is softer than previous study. We think this is the reason for the difference between our results and that of [Kegerreis et al. \(2018\)](#). The eroded mass of ice for small impact angle is smaller than that of hydrogen by an order of magnitude. In the case of low impact angle, both of HT and LT lose little water from core and impactor. However, the eroded water mass is more than the total mass of Uranian satellites. In the case of high impact angle, the impactor escapes from the target and the mass loss of water increases.

4. DISCUSSION

The eroded mass due to the collision can be understood by considering the heating area. Here we estimate the volume of ejected mass in terms of collision induced erosion volume V_{col} and shock induced erosion volume, V_{shk} , as

$$V_{\text{ej}} = V_{\text{col}} + V_{\text{shk}} \quad (7)$$

where

$$V_{\text{col}} = \sigma(R_p - R_c) \cos \theta \quad (8)$$

$$V_{\text{shk}} = \left[\frac{\pi}{6} h_1^2 (3R_p - h_1) - \frac{\pi}{6} h_2^2 (3R_c - h_2) \right] \quad (9)$$

$$- \left[\frac{\pi}{6} h_3^2 (3R_p - h_3) - \frac{2\pi R_c^3}{3} - \frac{4\pi}{3} (R_p^3 - R_c^3) \frac{\varphi}{2\pi} \right] \quad (10)$$

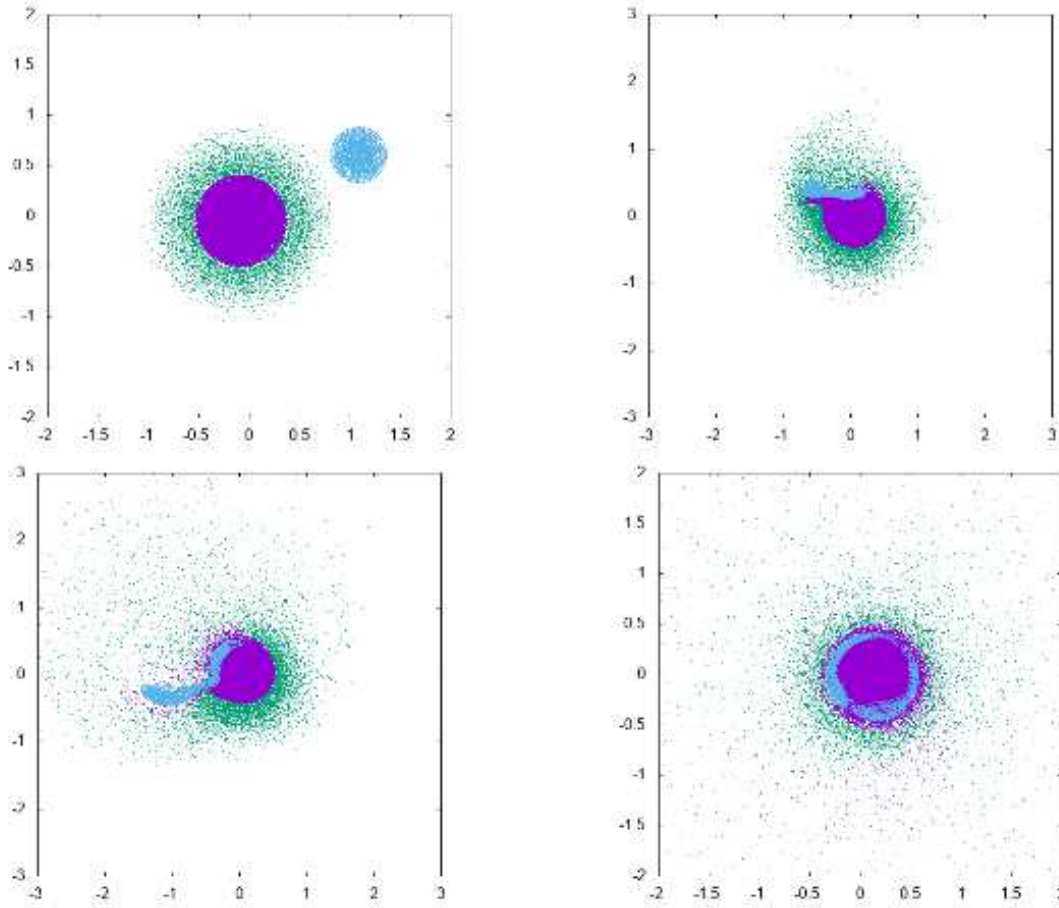


Figure 1. Snapshots of the high temperature target's impact simulation whose impact angle is $\theta = 30^\circ$. Green, purple, and blue dots represent target's hydrogen particles, target's water particles, and impactor's water particles, respectively. Those snapshots represent initial condition ($t = 0$), $t = t_{\text{ff}}$, $t = 2 t_{\text{ff}}$, and $t = 8 t_{\text{ff}}$ from top-left, top-right, bottom-left, and bottom-right, respectively, where t_{ff} is a free fall time.

where $h_1 = R_p + R_c \cos \varphi$, $h_2 = R_c + R_c \cos \varphi$, $h_3 = R_p + R_c$, $\varphi = \sin^{-1}[(R_p + r_{\text{imp}}) \sin \theta / R_c]$, R_c is the core radius of the target, and r_{imp} is the radius of the impactor (see Fig. 4). Thus, we can estimate the escaped mass as

$$M_{\text{esc},t} = \overline{\rho_{\text{env}}} V_{\text{area}} \quad (11)$$

where $\overline{\rho_{\text{env}}}$ is the averaged density. Since there is a strong negative gradient of density in hydrogen envelope, we adopt the bottom density of hydrogen envelope as the characteristic density. The density of hydrogen envelope $\approx 0.1 \text{ g} \cdot \text{cm}^{-3}$ at the core-envelope boundary for HT and LT. Here we assume $\overline{\rho_{\text{env}}} = 0.1 \text{ g cm}^{-3}$. When the impact parameter is large, a part of the impactor does not collide with the envelope of the target and then it does not fall onto the target. The impactor's loss $m_{\text{esc,imp}}$ can

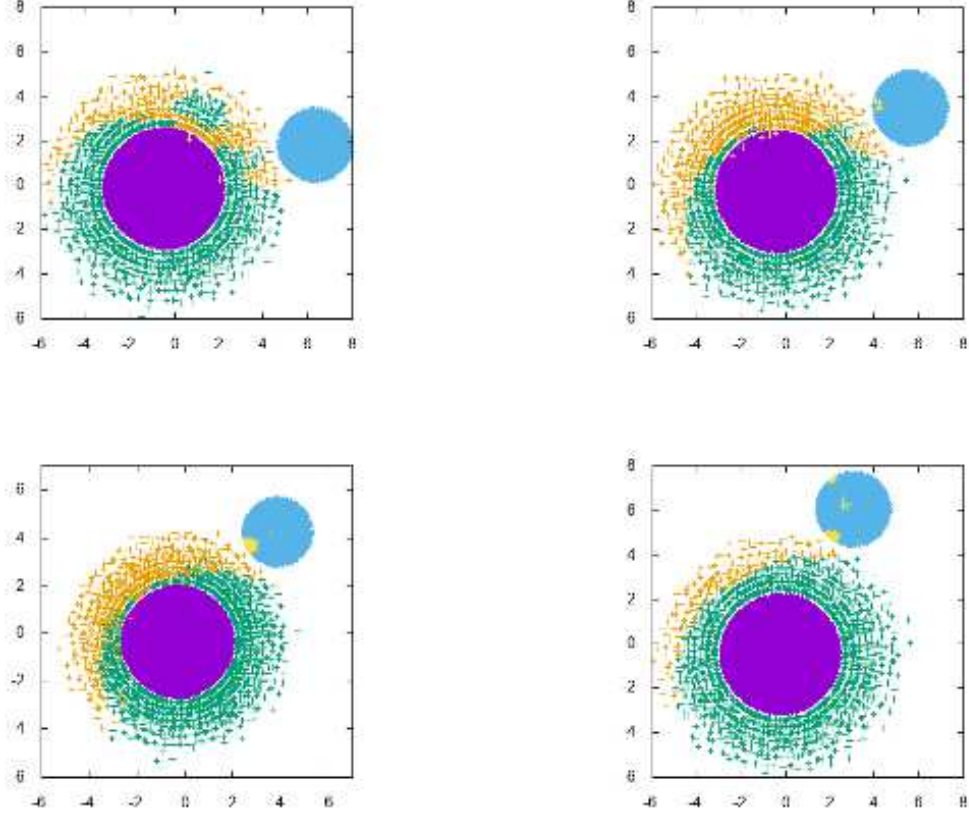


Figure 2. Ejected region for high temperature target. Only the particles close to the midplane ($-0.1 < z < 0.1$) are shown. Green, purple, and blue dots represent target’s hydrogen particles, target’s water particles, and impactor’s water particles, respectively. Orange and yellow dots shows eroded hydrogen and water particles, respectively. We represent different impact angles as follows. Top-left, top-right, bottom-left, and bottom-right represent 15° , 30° , 45° , and 60° , respectively. Those figures show a superposition of the initial state and the state after the collision.

be estimated as

$$m_{\text{esc,imp}} = \overline{\rho}_{\text{imp}} \pi r_{\text{imp}}^3 \left[\frac{2}{3} + \frac{(R_p + r_{\text{imp}}) \sin \theta - R_p}{r_{\text{imp}}} - \frac{1}{3} \left(\frac{(R_p + r_{\text{imp}}) \sin \theta - R_p}{r_{\text{imp}}} \right)^3 \right] \quad (12)$$

for $\sin \theta \geq \frac{R_p - r_{\text{imp}}}{R_p + r_{\text{imp}}}$. If $\sin \theta < \frac{R_p - r_{\text{imp}}}{R_p + r_{\text{imp}}}$, the entire impactor is expected to fall onto the target. That is, we set $m_{\text{esc,imp}} = 0$. Figure 5 also shows the analytical result. The analytical model can reproduce the trend of the relationship between the eroded mass and the impact parameter. However, the analytical model does not include the effect of the escape velocity, which should determine the difference between the HT and LT quantitatively. We suggest that it will be important to determine the propagation of three-dimensional shock wave in the interior of HT and LT.

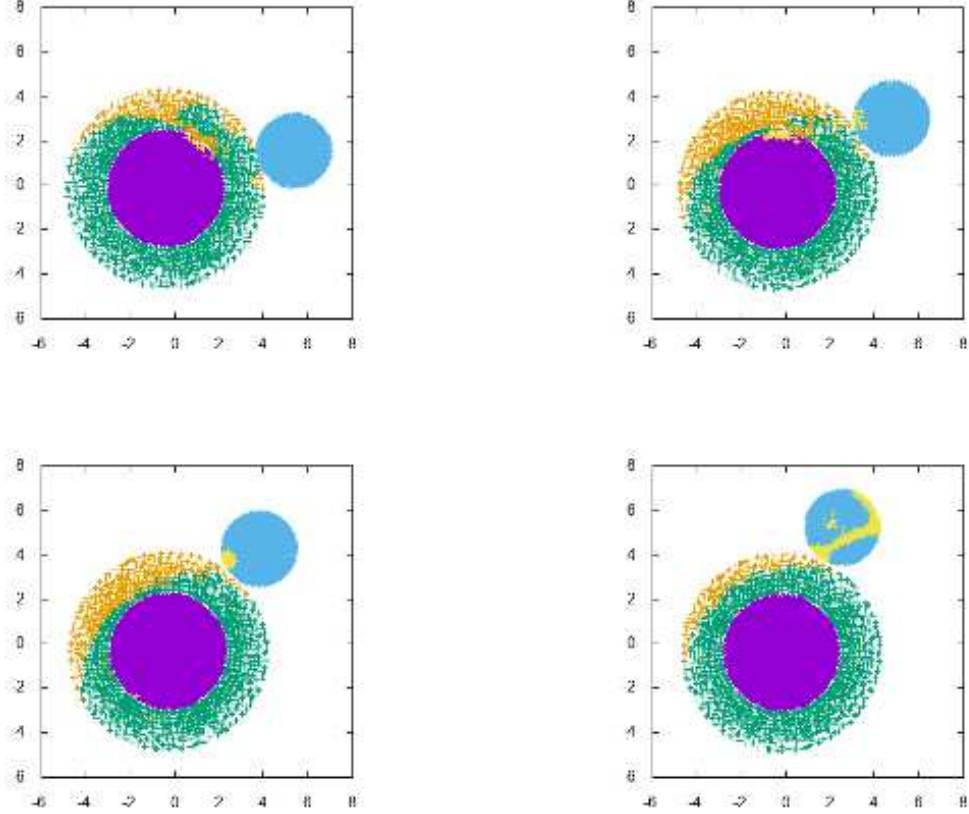


Figure 3. Same as Figure 2 but for LT target.

The total angular momentum that is transferred from the impactor to the target via collision is $L_{\text{tot}} (= m_{\text{imp}} v_{\text{imp}} (R_p + r_{\text{imp}}) \sin \theta)$. After the collision, the eroded mass and remove some fraction of the angular momentum that was given by the impactor. The angular momentum that is transferred thus

$$L_p = L_+ - M_{\text{esc,t}} v_{\text{ej}} R_c - m_{\text{esc,imp}} v_{\text{imp}} (R_p + r_{\text{imp}}) \sin \theta \quad (13)$$

where L_+ is transferred angular momentum to the target by the impactor and v_{ej} the ejecta velocity. Here we estimate v_{ej} by the impact ejecta scaling law (Melosh 1989; Richardson et al. 2005).

$$v_{\text{ej}} = \frac{2\sqrt{R_c g_s}}{1 + \varepsilon} \quad (14)$$

where g_s is the surface gravity, and ε is a material constant. When all the impactor particle are exist in $\theta > 0$, all particles moves counterclockwise after the impact that means L_+ is equal to L_{tot} . When $(R_p + r_{\text{imp}}) \sin \theta < r_{\text{imp}}$ is satisfied, some particles whose positions are $\theta < 0$ impact and reduce L_+ .

Here we divide the impactor to $\theta > 0$ and $\theta < 0$ region. V_1, V_2 are the volume of $\theta > 0$ and $\theta < 0$ region and h_1, h_2 are distance from the $x - z$ plane. Thus,

$$L_+ = \rho_{\text{imp}} v_{\text{imp}} [V_1(r_{\text{imp}} + (R_p + r_{\text{imp}}) \sin \theta - h_1) - V_2(r - (R_p + r_{\text{imp}}) \sin \theta - h_2)]. \quad (15)$$

Figure 6 shows the relationship between the obtained angular momentum and impact parameter. It shows that the angular momentum gain of the target is related to the eroded mass. The trend of the obtained angular momentum can be understood by Eq. 13. Moreover, the ejecta velocity is also understood by the ejecta scaling law (Eq. 14). The right panel of figure 6 shows the relationship for the obtained angular momentum normalized by present angular momentum of Uranus (Podolak & Reynolds 1987) and impact parameter. Our result suggests that HT case explain the present angular momentum of Uranus even if the impactor's mass is $1 M_{\oplus}$. If the target is in the high entropy state, the hydrogen envelope is expanded. Then the cross-section of proto-Uranus is enlarged and the angular momentum transported by the impactor is larger than in the LT case. We assumed that the initial hydrogen envelope is 20 %, which is larger than present Uranus. Venturini et al. (2016) implied that low- and intermediate-mass planets (mini-Neptunes to Neptunes) can be formed with total mass fractions of hydrogen up to 30 % considering the envelope polluted by ice materials. Thus, proto-Uranus might have had a more massive envelope than present Uranus because the target can loose envelope gas as a result of a giant impact.

4.1. Angular momentum transfer

Hyodo et al. (2017b) showed that the tidal disruption of a passing Kuiper Belt object is able to explain the formation of current ring and inner regular satellites of Uranus. On the other hand, previous studies (Slattery et al. 1992; Kegerreis et al. 2018) and our simulation suggest that a giant impact is also able to supply material to form regular satellites of Uranus. The total mass of major regular satellites around Uranus (Miranda, Ariel, Umbriel, Titania and Oberon) is $\sim 8.8 \times 10^{24}$ g (Brown et al. 1991), which is equivalent to 10^{-4} by Uranus's mass. Moreover, the total angular momentum of them is $\sim 10^{-2} \times L_U$. In this section, we consider the condition for particles that are bounded gravitationally and not fall onto the target after the impact. Those particles are supposed to be the origin of circumplanetary disk or ring.

Here we propose the criterion which determines the ejected particles will reaccrete or not by using the particle's orbital element. That is, they will no reaccrete if the pericenter distance of the i -th particle is longer than the target radius;

$$a_i(1 - e_i) > R_p \quad (16)$$

where a_i and e_i are semimajor axis and eccentricity of the i -th particle, respectively. a_i and e_i are calculated by

$$a_i = \left(\frac{2}{|\mathbf{x}_i - \mathbf{x}_g|^2} - \frac{|\mathbf{v}_i - \mathbf{v}_g|^2}{G(M_p + m_i)} \right)^{-1} \quad (17)$$

$$e_i = \sqrt{1 - \frac{|(\mathbf{x}_i - \mathbf{x}_g) \times (\mathbf{v}_i - \mathbf{v}_g)|}{G(M_p + m_i)a_i}} \quad (18)$$

where \mathbf{x}_g and \mathbf{v}_g are the position and velocity of the center of the gravity, respectively (cf. Murray & Dermott 1999). Figure 7 shows the particles which satisfy the condition of Eq 16. Our

result shows that particles satisfying Eq 16 and being bounded gravitationally exist in the case of $\theta = 45^\circ, 60^\circ$. Such particles mainly come from the impactor and their compositions are ice. Previous study (Slattery et al. 1992; Kegerreis et al. 2018) also demonstrated the same conclusion.

4.2. Implication for the satellite formation

In this study, the impact velocity is fixed to the escape velocity of the target, which means that all particles are bounded in the system gravitationally. The hydrogen envelope is eroded due to the momentum exchange with impactor. After that, the hydrogen envelope is scattered by the impact. Particles gravitationally unbound will escape, while the others will accrete onto the target.

On the other hand, some fraction of the impactor material and small amount of material blown out from the target do not accrete onto the target and remain in orbits around the target. During the impact event, hydrodynamical and tidal forces stretch the material, and then the angular momenta are exchanged by self-gravitational and hydrodynamical force. Figure 8 shows the time derivative of the particle’s angular momentum. Particles in the direction of moving transfer their angular momentum to particles behind them and then the orbital distances of the latter increase. If dL_z/dt are positive, particles should move outward because they gain angular momentum, while particles whose dL_z/dt are negative fall onto the target. Consequently, materials from the impactor are left around the target.

Figure 9 shows the particle mass which satisfy Eq. 16. Our simulation shows that an impact event can supply a sufficient amount of ices for the formation of the regular satellites. In the present simulation, we have adopted the impactor composed only of water, just for simplicity. In reality, the impactor should contain more or less rocky materials although the impactor’s ice-to-rock ratio is unknown. We expect that rocky material should also be ejected depending on the impact parameters, if we perform a simulation with the impactor that contains rocky material. However, the determination of the ejected material in the case of a rocky impactor is beyond the scope of the first paper in this line of our work. Comparing to Kegerreis et al. (2018), the mass in orbit according to our result is a factor of two lower. Our result also suggests that a LT target leads to a larger amount of material in orbit than a HT target does (Figure 9). Since the entropies of our targets are higher than assumed in Kegerreis et al. (2018), our results are consistent with that work.

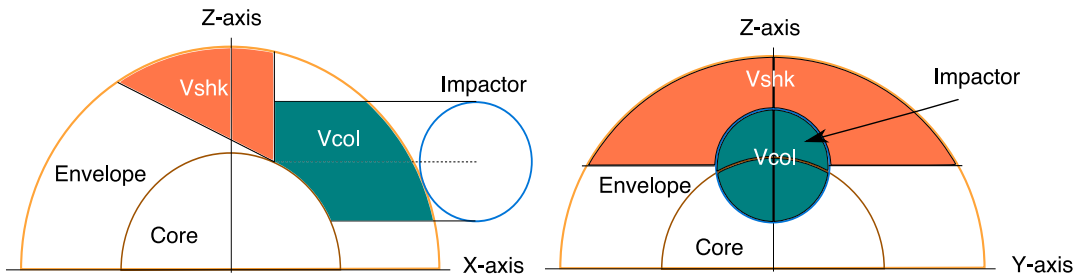


Figure 4. Panels show the estimated eroded region. The left and right panels show the V_{col} and V_{shk} on XZ-plane and YZ-plane, respectively. The green region shows V_{col} estimated by Eq. 8. The orange region shows V_{shk} estimated by Eq. 10.

5. CONCLUSION

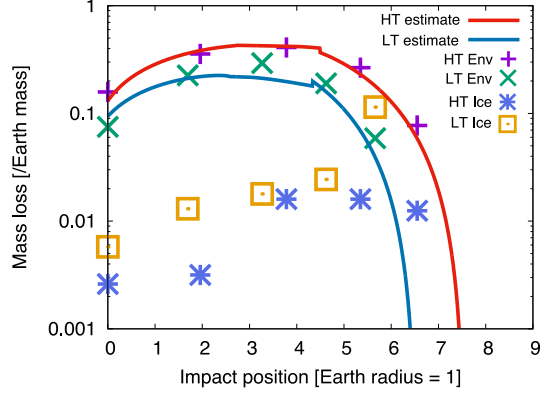


Figure 5. Relationship between the eroded mass and the impact parameter. The purple and green symbols represents the eroded hydrogen mass from the HT and LT, respectively. The dark blue and orange symbols represents the eroded water mass of HT+impactor and LT+impactor, respectively. The red and blue lines represent the analytical solution for the high temperature target and low temperature target derived by Eq. 11.

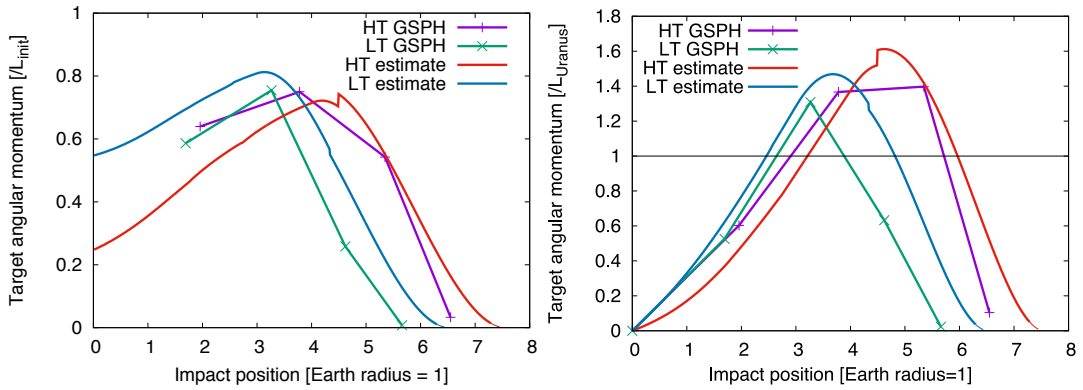


Figure 6. This figure shows the relationship between the obtained angular momentum and impact positions. The purple and green line represents the high temperature target and low temperature target, respectively. The Blue and orange lines represent the analytical solution for the high temperature target and low temperature target derived by Eq. 13. Left panel shows the efficiency of the transported angular momentum by a giant impact. Right panel shows the obtained angular momentum normalized by present angular momentum of Uranus (Podolak & Reynolds 1987).

In this paper we have performed numerical simulations of a giant impact on a young Uranus-like ice giant with Godunov SPH simulation with realistic structures composed of ice and hydrogen-helium gas in the case of no initial rotation of the target. We find that there is a relationship between the resultant mass loss and the angular momentum of the target. Our results suggest that a giant impact on proto-Uranus can explain the present value of the angular momenta of Uranus and its satellite system. We also find that if the target is in high entropy state, it obtains larger angular momentum and lose its envelope more efficiently than the low entropy state, because the hydrogen envelope of the high entropy target is significantly more extended. Our results also show that less mass remains gravitationally bound in high entropy target than in a low entropy target. Our results may provide a step forward to understand the origin of Uranus.

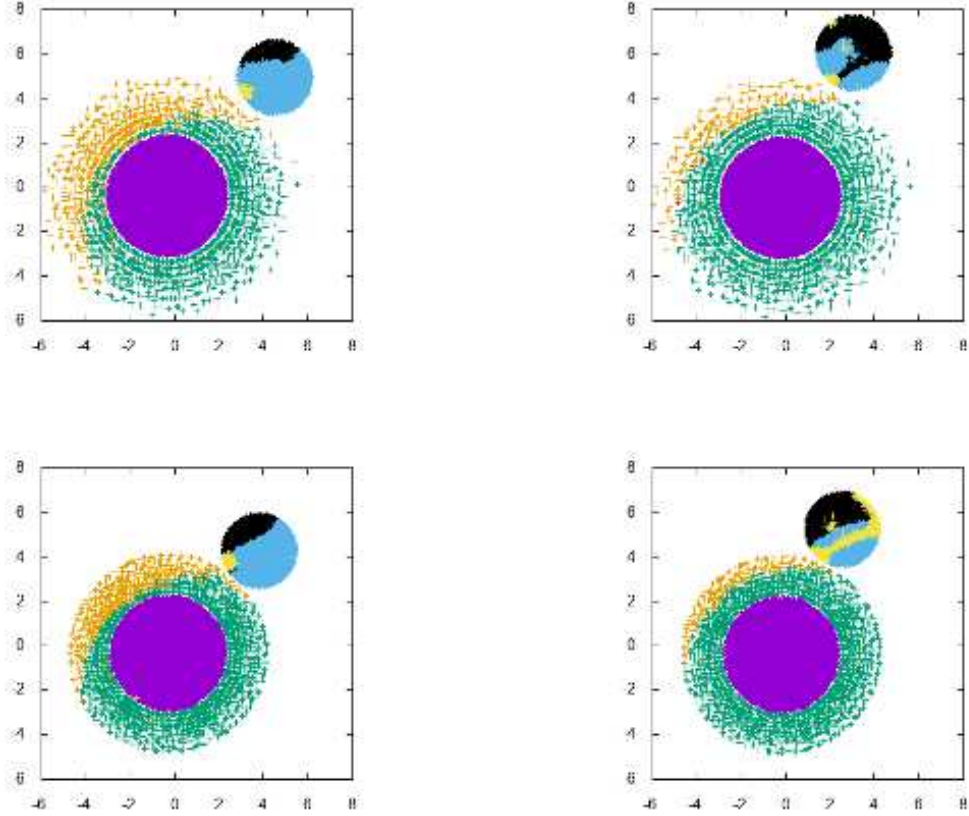


Figure 7. Particles that become the circum-planetary disk are shown with different colors in the initial condition. Only the particles close to the midplane ($-0.1 < z < 0.1$) are shown. The color code is the same as Figures 2,3 except that in addition, red and black dots shows hydrogen and water particle that satisfy Eq 16, respectively. In our simulation, most of the hydrogen particles which satisfy Eq 16 also satisfy Eq 5. That is, those particle should eroded, which shown in orange dots. Thus the number of red particles are very small in this representation. Left-top and right-top figure shows the result of HT target whose impact angles are 45° (left-top) and 60° (right-top), respectively. Left-bottom and right-bottom figure show the result of LT target whose impact angles are 45° (left-bottom) and 60° (right-bottom), respectively.

KK thanks Y. Guo and K. Sugiura for discussions on GSPH method. He also thanks N. Hosono and D. Namekata for the use of FDPS. The authors also thank K. Iwasaki, S. Takasao, and H. Kobayashi for fruitful comments. Numerical computations were carried out on Cray XC30 at Center for Com-

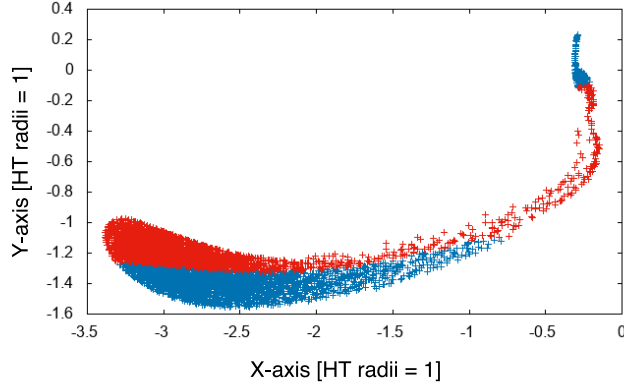


Figure 8. The transport of angular momentum via self-gravity. This snapshot is taken $3 t_{\text{ff}}$ after the collision for the case of the impact angle 60° on HT target. The color shows the time derivative of the angular momentum due to the gravitational force. Red and blue show $dL_z/dt > 0$ and $dL_z/dt < 0$, respectively.

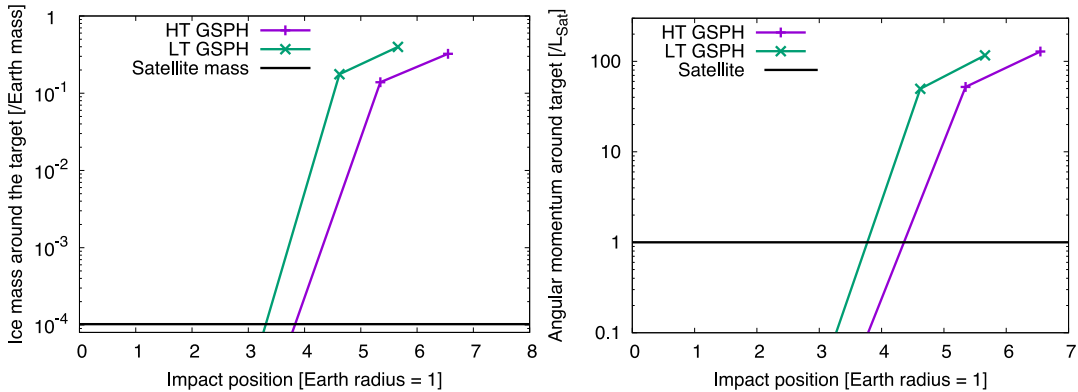


Figure 9. Relationship between the impact angle and total water particles mass (left panel) and their angular momentum (right panel) in the circum-planetary disk. Purple and red lines represent the high temperature target, while green and blue lines are low temperature target, respectively. The black line shows the total mass and angular momentum of regular satellite of Uranus.

putational Astrophysics, National Astronomical Observatory of Japan. This work was supported by JSPS KAKENHI Grant Numbers 16H02160.

APPENDIX

A. RIEMANN SOLVER FOR GODUNOV SPH WITH SELF-GRAVITY

In this appendix, we introduce the Riemann solver for our GSPH (see also Guo et al. 2018). Here we consider the Riemann solver for i and j particles. The expression for the result of Riemann

problem we use is

$$p^* = \frac{p_i/W_i + p_j/W_j - v_i + v_j}{1/W_i + 1/W_j} \quad (\text{A1})$$

$$v^* = \frac{v_i W_i + v_j W_j - p_i + p_j}{W_i + W_j} \quad (\text{A2})$$

where p, v are pressure, and velocity, respectively. W_k abbreviates

$$W_k = \sqrt{\gamma p_k \rho_k} \sqrt{1 + \frac{\gamma + 1}{2\gamma} \frac{p^* - p_k}{p_k}} \quad \text{for } p^* \geq p_k \quad (\text{A3})$$

$$W_k = \sqrt{\gamma p_k \rho_k} \frac{\gamma - 1}{2\gamma} \frac{1 - p^*/p_k}{1 - (p^*/p_k)^{(\gamma-1)/(2\gamma)}} \quad \text{for } p^* < p_k \quad (\text{A4})$$

where γ, ρ are the ratio of specific heats and density, respectively. To take into account the gravitational force \mathbf{F}_g on Eq. A1 and A2, we replace p_i and p_j with p'_i and p'_j as shown in the following:

$$p'_i = p_i - \frac{1}{2} \rho_i C_{s,i} \mathbf{F}_g \cdot \hat{s} \delta t \quad (\text{A5})$$

$$p'_j = p_j + \frac{1}{2} \rho_j C_{s,j} \mathbf{F}_g \cdot \hat{s} \delta t \quad (\text{A6})$$

where $C_{s,k} = \sqrt{\gamma_k p_k \rho_k}$, $\hat{s} = (\mathbf{x}_i - \mathbf{x}_j)/|\mathbf{x}_i - \mathbf{x}_j|$ and δt is the time step.

B. THERMAL EVOLUTION OF THE TARGET

In this appendix, we briefly explain the thermal evolution of the target. The target is composed of 80 % of water core surrounded by 20 % of hydrogen-helium atmosphere. We numerically integrate the thermal evolution. We assume the target consists of three layers in spherical symmetry and hydrostatic equilibrium, that include, from top to bottom (1) a radiative-convective equilibrium atmosphere composed of hydrogen helium, (2) a convective equilibrium envelope composed of hydrogen helium, and (3) a convective equilibrium water-ice core. Details of atmosphere, interior, and thermal evolution model are described in Kurosaiki & Ikoma (2017). Figure 10 shows the thermal evolution of the target. Purple line shows an ice giant whose hydrogen-helium atmosphere is free from ice materials, while green line shows the case with atmosphere is mixed with ice materials by 50 % by mass. The temperature at 1 bar of present Uranus is ~ 80 K. Temperatures at 1 bar for HT and LT target are 270 K and 120 K, respectively. HT and LT correspond to 1.6×10^8 years and 2.3×10^9 years, respectively. As previous studies (Fortney et al. 2011; Nettelmann et al. 2016) indicated that Uranus could imply strong barrier to interior convective cooling. Kurosaiki & Ikoma (2017) suggested that an ice-rich atmosphere can accelerate the cooling due to the effect of the condensation in the atmosphere, though it requires 50 % of ice by mass. Our target assume an ice giant with ice-free atmosphere. In our model, the target in Kegerreis et al. (2018) may corresponds to an evolved ice giant with ice-rich atmosphere. Therefore, we are proposing that if HT target's interior is mixed with ice efficiently after the impact, subsequent thermal evolution of HT can reproduce present Uranus. However, the detailed determination of the amount of mixing by the impact is beyond the scope in this study.

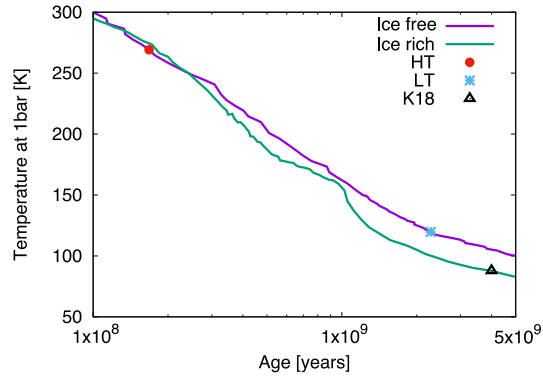


Figure 10. Relationship between the age and the temperature at 1 bar. Purple and green lines represent thermal evolution of ice giants whose ice mass fractions in the atmosphere are 0 wt% and 50 wt% (ice rich), respectively. The red and blue means HT and LT target conditions, respectively. The condition for Kegerreis et al. (2018) is represented black (K18 in the figure), which corresponds to the present Uranus.

C. THE DETERMINATION OF UNBOUND PARTICLES: THE EFFECT OF THE INTERNAL ENERGY

We check the effect of the internal energy on the determination of unbound particles. The condition that the particle’s velocity exceeds the escape velocity (hereafter CRT1) is Equation 5. On the other hand, the particle’s internal energy increase after the impact event. The larger internal energy causes the larger pressure to the particle. Thus the pressure gradient may accelerate the particle and contribute to its escape. We include the internal energy into the condition, Equation 5;

$$m_i u_i + \frac{1}{2} m_i |\mathbf{v}_i|^2 - m_i \sum_{i \neq j} \frac{G m_j}{|\mathbf{r}_i - \mathbf{r}_j|} > 0, \quad (C7)$$

and hereafter we call this condition, CRT2. Figure 11 shows the relationship between the eroded mass and the impact parameter. We find that the eroded mass of CRT2 is larger than that of CRT1. When the impact occurs, the particle’s internal energy is increased because the impact event distributes the kinetic energy to the internal energy of the particles. After the impact, the hydrodynamic motion redistributes the particle’s internal energy to the kinetic energy (cf. Genda et al. 2015). That is, the pressure gradient caused by the internal energy accelerates the particles. However, the difference of the eroded mass between CRT1 and CRT2 is less than 5 %. Therefore, we adopt CRT1 as the condition of unbound particles.

REFERENCES

- | | |
|---|--|
| Brown, R. H., Johnson, T. V., Synnott, S., et al. 1991, <i>Uranus</i> , 513 | Fortney, J. J., Ikoma, M., Nettelmann, N., Guillot, T., & Marley, M. S. 2011, <i>ApJ</i> , 729, 32 |
| Cameron, A. G. W., & Ward, W. R. 1976, <i>Lunar and Planetary Science Conference</i> , 7, 120 | Guo, Y., Inutsuka, S., & Tsuribe, T. submitted to <i>ApJ</i> |
| Cha, S.-H., Inutsuka, S.-I., & Nayakshin, S. 2010, <i>MNRAS</i> , 403, 1165 | Genda, H., Kokubo, E. & Ida, S. 2012, <i>ApJ</i> , 744, 137. |
| Citron, R. I., Genda, H., & Ida, S. 2015, <i>Icarus</i> , 252, 334 | Genda, H., Fujita, T., Kobayashi, H., Tanaka, H., & Abe, Y. 2015, <i>Icarus</i> , 262, 58 |

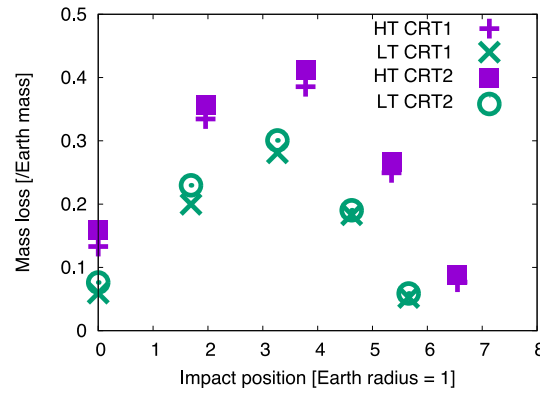


Figure 11. Relationship between the eroded mass and the impact parameter. Purple and green symbols represent the high temperature target and low temperature target using criterion CRT1 (squares, circles) or CRT2 (crosses, pluses).

- Hartmann, W. K., & Davis, D. R. 1975, *Icarus*, 24, 504
- Helled, R., Anderson, J. D., Podolak, M., & Schubert, G. 2011, *ApJ*, 726, 15
- Hubbard, W. B., & Macfarlane, J. J. 1980, *J. Geophys. Res.*, 85, 225
- Hyodo, R., Rosenblatt, P., Genda, H., & Charnoz, S. 2017, *ApJ*, 851, 122
- Hyodo, R., Charnoz, S., Ohtsuki, K., & Genda, H. 2017, *Icarus*, 282, 195
- Imaeda, Y., & Inutsuka, S.-i. 2002, *ApJ*, 569, 501
- Inutsuka, S.-I. 2002, *Journal of Computational Physics*, 179, 238
- Iwasawa, M., Tanikawa, A., Hosono, N., et al. 2016, *PASJ*, 68, 54
- Kegerreis, J. A., Teodoro, L. F. A., Eke, V. R., et al. 2018, *ApJ*, 861, 52
- Kurosaki, K., & Ikoma, M. 2017, *AJ*, 153, 260
- Korycansky, D. G., Bodenheimer, P., Cassen, P., & Pollack, J. B. 1990, *Icarus*, 84, 528
- Lyon, S. P., & Johnson, J. D. 1992, Los Alamos National Laboratory, Los Alamos, NM, LA-UR-92-3407
- Marcus, R. A., Stewart, S. T., Sasselov, D., et al. 2009, *ApJ*, 700, L118.
- Melosh, H. J. 1989, Research supported by NASA. New York, Oxford University Press (Oxford Monographs on Geology and Geophysics, No. 11), 1989, 253 p., 11
- Monaghan, J. J. 2006, *MNRAS*, 365, 199
- Murray, C. D., & Dermott, S. F. 1999, *Solar system dynamics* by C.D. Murray and S.F. McDermott. (Cambridge, UK: Cambridge University Press), ISBN 0-521-57295-9 (hc.), ISBN 0-521-57297-4 (pbk.).
- Namekata, D., Iwasawa, M., Nitadori, K., et al. 2018, *PASJ*,
- Nettelmann, N., Wang, K., Fortney, J. J., et al. 2016, *Icarus*, 275, 107
- Parisi, M. G., & Brunini, A. 1997, *Planet. Space Sci.*, 45, 181
- Parisi, M. G., Carraro, G., Maris, M., & Brunini, A. 2008, *A&A*, 482, 657
- Podolak, M., & Reynolds, R. T. 1987, *Icarus*, 70, 31
- Richardson, J. E., Melosh, H. J., Artemeiva, N. A., & Pierazzo, E. 2005, *SSRv*, 117, 241
- Safronov, V. S. 1966, *Soviet Ast.*, 9, 987
- Saumon, D., Chabrier, G., & van Horn, H. M. 1995, *ApJS*, 99, 713
- Slattery, W. L., Benz, W., & Cameron, A. G. W. 1992, *Icarus*, 99, 167
- Sugiura, K., & Inutsuka, S.-i. 2016, *Journal of Computational Physics*, 308, 171
- Venturini, J., Alibert, Y., & Benz, W. 2016, *A&A*, 596, A90